Development of colorimetric lateral flow assays with gold nanostructures for Cystatin C detection

Sensors and Actuators Reports 4 (2022) 100121

Contents lists available at ScienceDirect

Sensors and Actuators Reports

journal homepage: www.sciencedirect.com/journal/sensors-and-actuators-reports

Development of colorimetric lateral flow assays with gold nanostructures for Cystatin C detection

Xushuo Zhang [a], Sam Fishlock [a], Peter Sharpe [b], James McLaughlin [a,*]

[a] Nanotechnology and Integrated Bioengineering Centre (NIBEC), Ulster University, Jordanstown, BT37 0QB, UK
[b] Clinical Biochemistry Laboratory, Southern Health and Social Care Trust, Portadown BT63 5QQ, UK

ARTICLE INFO

Keywords:
Gold nanostructures
Cystatin C
Renal biomarker
Lateral flow assay
Sensitivity
Colorimetric

ABSTRACT

Cystatin C (CysC) is a biomarker indicative of renal function, and its comorbidities, including heart failure. Generally, enzyme-linked immunosorbent assay (ELISA) can detect CysC in hours but requires skilled personnel, thorough reagent preparation, and a laboratory setting. Here, we report quantitative lateral flow immunoassays (LFIAs) with two gold nanostructures (AuNSs): gold nanoparticles (AuNPs) and gold nanorods (AnNRs). UV–Vis suggests 358 μg/ml mAbs in AuNPs conjugation and 45 μg/ml mAbs in AuNRs conjugation. With dynamic light scattering (DLS) measuring the hydrodynamic radius (R_h) of monoclonal antibodies (mAbs) – AuNSs conjugates, AuNPs conjugate maximum R_h is 125.9 ± 11.6 nm (1074 μg/ml conjugated mAbs). 895 μg/ml mAbs – AuNRs conjugate gives maximum R_h (55.9 ± 4.5 nm), but 45 μg/ml AuNRs conjugate displays optimum LFIAs performance. Wash-step and bridged structures were introduced for a wider linear range of CysC quantification (up to 12.5 mg/L), with AuNPs' limit of detection (LoD) as 0.42 mg/L (wash-step), 0.87 mg/L (bridged structure) and AuNRs LoD as 0.35 mg/L. AuNRs are therefore more sensitive than AuNPs however the test line signal intensity suggests AuNPs are visually stronger. Furthermore, with the drawbacks of the bridged structure's complex fabrication and wash-step dipstick format's multi-steps, conventional LFIAs with AuNPs (89.5 μg/ml mAbs) conjugate in 10 min turnaround time were developed (LoD: 1.04 mg/L). Intra- assay CV% and inter- assay CV% are 13.69% 21.75%, accordingly. Human samples were then tested to address the matrix effect, with an average recovery rate of 99.37 ± 2.23% and an average CV% of 2.81%.

1. Introduction

Cystatin C (CysC) is a biomarker indicating renal function and is closely related to heart failure due to cardiorenal syndrome. The cardiorenal syndrome is a reciprocate impairment between the heart and kidney [1] starting from venous pressure rising and involving the renin-angiotensin-adulterine system. CysC is favoured in predicting a small reduction in glomerular filtration rate compared with creatinine, and this is certified by the recent reference looking into the prediction of long-term mortality [2]. Glomerular filtration rate (GFR) is an indicator of the overall index of renal function [3]. Since it is the amount of blood glomerulus filtering per minute, it is generally estimated by the concentrations of exogenous markers including CysC. With CysC also an indicator for acute kidney injury [4], ischaemic stroke [5], and carotid atherosclerosis [6], it is essential to monitor serum CysC levels between 0.5 and 10 mg/L [7].

Presently, the measurement of CysC level is conducted by ELISA, turbidimetric, and nephelometric immunoassays [8]. Nephelometric and turbidimetric approaches, as standards for CysC measurements, demand professionally analytical instruments and processing units [9]. These methods, including ELISA, are time-consuming [8,10] and require specialized technicians [11]. As a result, rapid assays at point-of-care LFIAs are developed to streamline patient care by providing diagnostic and detection values within a short turnaround time. Our work, in this regard, develops a colorimetric LFIAs biosensor for CysC levels interpretation in 10 min. Though fluorescent dye is deployed in LFIA development for CysC detection [12], it relies on extra excitation sources compared to colorimetric assays [13,14]. Recent developments in AuNSs synthesis, such as gold nanoparticles (AuNPs) and nanorods (AuNR) geometries, promise significant varieties in assay formats due to their plasmonic resonant traits [15].

Nanostructures have been widely used in disease prognosis. Specifically, the Au nano-pyramid has been used in the detection of S-100β, a traumatic brain injury biomarker in blood plasma, whereby the paper-

* Corresponding author.
E-mail address: jad.mclaughlin@ulster.ac.uk (J. McLaughlin).

https://doi.org/10.1016/j.snr.2022.100121
Received 15 April 2022; Received in revised form 31 August 2022; Accepted 7 September 2022
Available online 13 September 2022

based LFIAs enabled the rapid detection among traumatic brain injury patients [16]. Similarly, gold nanoshells were deployed in thyroid-stimulating hormone (TSH) quantitative LFIAs [17]. With the advanced decoration of the nanostructures, their sensitivity in the detection of infectious diseases p24 (HIV-1 capsid), Escherichia coli, and SARS-CoV-2 [18] and agricultural food safety by monitoring furazolidone [19] was improved compared with traditional AuNPs. The combination of nanostructures Au-Ag cubit nanocages was introduced for human prostate-specific antigen detection [20]. Specifically, for CysC detection, a dual-signal readout with colorimetric and fluorescent signals for CysC detection was found to enhance the detection sensitivity of real human serum samples compared with conventional LFIAs [13]. To synthesize the Au-Ag nanocages, silica templates with dendritic supporting silica layers with an average diameter of 270 nm and pore width of 40 nm, AuNPs with an average diameter of 12 nm capping by oleylamine were implanted via thiol and metal affinity force. Subsequently, the nanostructure was filled by a silica matrix until a smooth layer of 30 nm silica shell formed. This layer prevented the potential agglomeration between AuNPs and quantum dots, which later immobilized as a dense layer outside the 30 nm shell. After the ultimate bilayer encapsulation by the organosilica, the dual model is formed for CysC colorimetric and fluorescence detection. The linear range of the fluorescence mode is up to 0.01563 mg/L, with the LoD as 0.24×10^{-3} mg/L, this is far lower than the CysC level in healthy individuals [3,21]. Plus, the costly and complex structures are another drawback of these nanostructures [22]. Additionally, such a multi-stage process may be uncontrollable, might be resulting in the non-specific binding of proteins on metals and the irreproducibility from batch to batch [15]. Moreover, the additional drawback of fluorescence and quantum dots is the relatively complicated quantification system setups, since lasers and laser diodes are required to excite fluorophores and quantum dots, and dichroic or emission filters are needed to block the unnecessary light [23]. While fluorescence had been used in heart-type fatty acid binding protein (H-FABP) detection with decorated quantum dots at the test line changing from green to red in presence of the analyte [24]. With the wide application of LFIAs in the detection of Salmonella typhimurium [25], exosomes as non-invasive cancer biomarkers [26], SARS-CoV-2 [27,28], inflammatory biomarker C - reactive protein [29], bacteria [30], and acute myocardial infarction's biomarker cardiac troponins [31], paper-based point-of-care demonstrates the applicability in aspects of daily life and healthcare. Whilst the conjugation of mAbs with AuNSs is ubiquitous [32] and widely used in recent SARS-CoV-2 detection [27,28], we aim to address the optimized mAbs and AuNS conjugation and developed LFIAs for clinical range CysC detection in this work.

Hook effects commonly exist in LFIA development [33]. The hook effect is a factor leading to false-negative diagnostics results. It describes a higher concentration analyte giving out an identical signal to a low concentration analyte. Research back in 1947 [34] firstly discovered high concentration analyte leading to low diagnostics signals. Besides saturation of antibody binding at the test line, research in 2004 suggests the competition binding between free sample analyte and bounded sample analyte leads to the hook effect [35]. Specifically, if the free analyte travels up to bind the immobilized antibodies on the test line, then the bounded analyte (analyte captured by detector antibody conjugated on the AuNSs surface) could not bind thus leading to the de-coloration of the test line. Research also found that diluted samples could give out stronger diagnostics signals compared with undiluted samples [36]. To avoid the hook effects, bridged structures [37] and controlled conjugate release methods [38] were introduced to enable the washing step, which washed off the free analyte at the test line before the release of the AuNSs.

2. Material and methods

2.1. AuNSs antibody complex conjugation

AuNPs were obtained from Abcam (Gold-carboxyl nanoparticles, Abcam) as a 40 nm AuNPs conjugation kit (40 nm, 40 OD, ab269942). Detector mAbs (10–7887, Fitzgerald) from 5 μg/ml to 1611 μg/ml were conjugated to the AuNPs following the kit's conjugation instructions. Specifically, diluting antibodies in 10 mM MES to have the ideal concentration of antibody solutions ready to be conjugated, then adding the 20 μl solution into 10 μl 100 mM MES. With additional 50 μl GNPs in to have the total volume of 80 μl, 20 μl 1 mM EDC were added into 80 μl mixtures to have a total volume of 100 μl. Incubate this 100 μl on a roller for 20 min while rotating. After incubation, adding 1 ml of 1×TBS pH 8.0, 0.05% Tween 20. Mix well and centrifuge down at 7000 RPM for 10 min. Discard the supernatant and tap the pellets, then adding 90 μl of 1×TBS pH 8.0, 0.05% Tween 20, 0.5% BSA to obtain OD 20 GNPs. Conjugation was completed at optical density (OD) 20 AuNPs and this 100 μl was further diluted into 400 μl OD 5 with conjugate diluent 1x TBS pH 8.0 with 0.05% Tween 20 and 0.5% BSA.

AuNRs conjugation was conducted from PEG carboxyl particle covalent conjugation (PEG Carboxyl gold nanorods 55 nm × 15 nm, OD 50 in water, nanoComposix). Similarly, detector mAbs (10–7887, Fitzgerald) in concentrations from 5 μg/ml to 1432 μg/ml were conjugated to the AuNRs following the conjugation kit's manual, conjugation details are summarised in the supporting information. OD 15 was achieved and dilution into OD 5 with the addition of 0.01× PBS and 0.5% PEG 20,000 kDa, pH 7.4.

2.2. UV-vis spectra of mAbs conjugated AuNSs

UV-vis absorbance spectra of AuNPs and AuNRs were recorded via the spectrometer LAMBDA™ 365 (PerkinElmer, UK). Specifically, mAbs – AuNPs conjugates were measured at wavelengths between 480 nm and 580 nm, and 750 nm to 880 nm for AuNRs. Quartz cuvettes with a path length of 0.1 cm and inside width of 1 cm were used in the process of measurements.

2.3. Dynamic light scattering (DLS) hydrodynamic size measurement

DLS of mAbs conjugated AuNSs' analysis was carried out with Zetasizer Nano ZS (Malvern Panalytical Ltd, UK). Size measurements are based on light scattered by the particles inside the cuvette. The attenuator was automatically adjusted during the time of the measurements to give out the proper kilo-counts per second (kcps). The diluted sample should reach at least 10 kcps and sample concentrations should be a minimum of 30% excess scattering over the solvent. If solvent acquires 110 kcps, sample concentration is demanded to reach 110 kcps × 1.30, 143 kcps. mAbs conjugated AuNSs were diluted in 10 mM NaCl with a 1:100 dilution factor, with a cell temperature set as 22 °C and appropriate equilibration time. Equilibration time is the time needed to reach the set temperature. There is also a delay when the cell area temperature has reached the requested temperature, as this delay tries to make sure the cuvette liquid temperature is equilibrated with the cell area temperature. Ensuring the temperature equilibrated inside the cell allows the sample to be measured under Brownian motion instead of thermal motion. The duration of measurement was set to '1 run' with each run duration lasting for 360 s, with 3 measurements for each sample.

2.4. LF assembling and LFIAs

The conjugate pad was pre-treated with 10 mM PBS, 5% sucrose, and 1% BSA, 0.5% Tween-20 via Biodot's Airjet and the printing speed was 10 μl/cm. Similarly, the sample pad was pre-printed via Biodot's Airjet with 0.25 M tris-aminomethane (Sigma-Aldrich), 0.1% BSA, 0.1% Tween 20, and 0.1% sodium azide [39]. The printing speed remained 10

μl/cm. After pre-treatment, the conjugate pad and sample pad were dried at 37 °C (with less than 1% humidity) for at least 2 h before use. Then, the conjugate pad was printed with AuNSs via Biodot's Airjet with a printing speed of 10 μl/cm. The AuNSs printed conjugate pads were dried for 2 h at 37 °C (with less than 1% humidity).

Nitrocellulose (NC) membranes CN 95 were used, and printing was via the Biodot's syringe pumps. Both the control line antibody goat anti-mouse IgG1 (Fitzgerald, 20R-IG003-FIT) and capture antibody (Fitzgerald, 10–7886) were in 1 mg/ml concentrations, with a printing speed of 1 μl/cm and 0.5 cm gap between the test line and the control line. Then the NC membrane was dried under 37 °C and less than 1% humidity for at least 2 h before use.

The bridged structure was assembled with blank NC membranes being immobilized on top of a polystyrene backing card. The NC membrane containing the control and test lines was placed above the blank NC membrane on the backing card. A 3 mm gap was designed to keep away from the blank NC membrane. The absorbent pad was then adhered on top of the backing card, above the NC membrane containing test and control lines. A pre-treated sample pad was placed on top of the 3 mm gap on the backing card. Meanwhile, the buffer pad was placed at the end of the backing card with 2 mm overlapping with the blank NC membrane. Finally, 2 untreated sample pads were placed on top of the blank NC membrane, with a conjugate pad containing sprayed AuNSs being placed on top of the two untreated sample pads. See Fig. 1(a) below. LFIA tests were conducted with 0.5 μl CysC (0.1 mg/L – 12.5 mg/L) on the pre-treated sample pad and then 59.5 μl running buffer on the buffer pad. CysC used is CysC protein (30R-3194-FIT, Fitzgerald, USA) dissolved in PBS medium upon purchase. Test strips were scanned after 10 min ($t = 10$ min). Here, standard LFIA strips assembly was followed as in Fig. 1b. To address the intra- and inter- assay comparison and matrix effect, the LFIAs with 2.5 μl sample volume, AuNSs on the pre-treated conjugate pad, and 60 μl running buffer were conducted without the involvement of wash step in between. Lyophilized CysC protein (30R-AC035-FIT, Fitzgerald, USA) was spiked in the PBS medium. Human serum samples were provided by Southern Health and Social Care Trust with CysC concentrations validated from Roche Cobas modular system.

Standard dipstick assay format is shown in Fig. 2(a), with a sum volume of CysC, AuNSs conjugate, and running buffer as 60 μl, and all are added simultaneously. Fig. 2b shows the diagram of having a wash-step before adding mAbs conjugated AuNSs. The washing step usually mitigates false-negative results in point-of-care assays [40]. Additionally, running buffer used in the LFIA are two types with different percentage of BSA: 10 mM PBS + 0.1% Tween + 1% BSA or 10 mM PBS + 0.1% Tween + 2% BSA.

2.5. Lumos reader for LFIA strips results in interpretation

The Lumos Benchtop Reader (Lumos Diagnostics, CA, USA) was used for LFIA color intensity reading and interpretation. An LFIA strip can be scanned as an image with the lines' intensity projected above the image, see Fig. 3. After loading the sample and applying running buffer, the strips were read after 10 min. Quantitation of the test and control lines was performed via red light illumination, with a 3-ms exposure. Peaks of control and test lines were centered at 600 pixels and 750 pixels respectively with 30 pixels tolerance. The background was set on two sides of the peaks. On the left: 450 pixels – 500 pixels, on the right: 850 pixels – 900 pixels. The heights of the peaks were then recorded, corresponding to each CysC concentration.

3. Results and discussion

3.1. Optimal mAbs concentration for AuNSs' conjugation

Detection of CysC was achieved by conjugating the AuNSs with mAbs selective to CysC. UV-vis had been denoted as an efficient method to appraise biomolecule – AuNSs' conjugates [42]. We synthesized the mAbs – AuNPs conjugates with chosen mAb concentrations of 45, 89.5, 100, 358, and 895 μg/ml. Fig. 4(a) records the UV-vis spectra of OD 10 AuNPs in a 0.1 cm path length cuvette and indicates a 3 nm redshift with the increase of mAbs concentration (45 μg/ml to 895 μg/ml), with the maximum absorbance shifts from 527 nm to 530 nm, Fig. 4(a). We, therefore, performed LFIAs with multiple concentrations of mAbs – AuNPs to detect CysC in concentrations of 0.5, 0.8, 1, 2.5, 4, and 5 mg/L. The 358 μg/ml mAbs – AuNPs conjugate shows a greater extent of signal intensities among all five concentrations mAbs – AuNPs conjugates, Fig. 4(b). Accordingly, UV-vis's spectra of AuNRs' conjugates undergo a 5–10 nm redshift from 812 nm to 819.5 ± 2.5 nm (Fig. 4c). mAbs concentrations 45, 133.3, 179, 537 and 895 μg/ml were conjugated with AuNRs (OD 15), and CysC concentrations 0.1, 0.25, 0.5, 0.8, 1, 2.5, 4 and 5 mg/L were evaluated via LFIAs (Fig. 4d). Five mAbs – AuNRs OD 15 conjugates illustrate similar signal intensities, as results of LFIAs performance of these mAbs – AuNRs' conjugates are evenly distributed in Fig. 4(d).

358 μg/ml mAbs – AuNPs conjugate produces the maximum absorbance among five mAbs – AuNPs' conjugates and this conjugate also

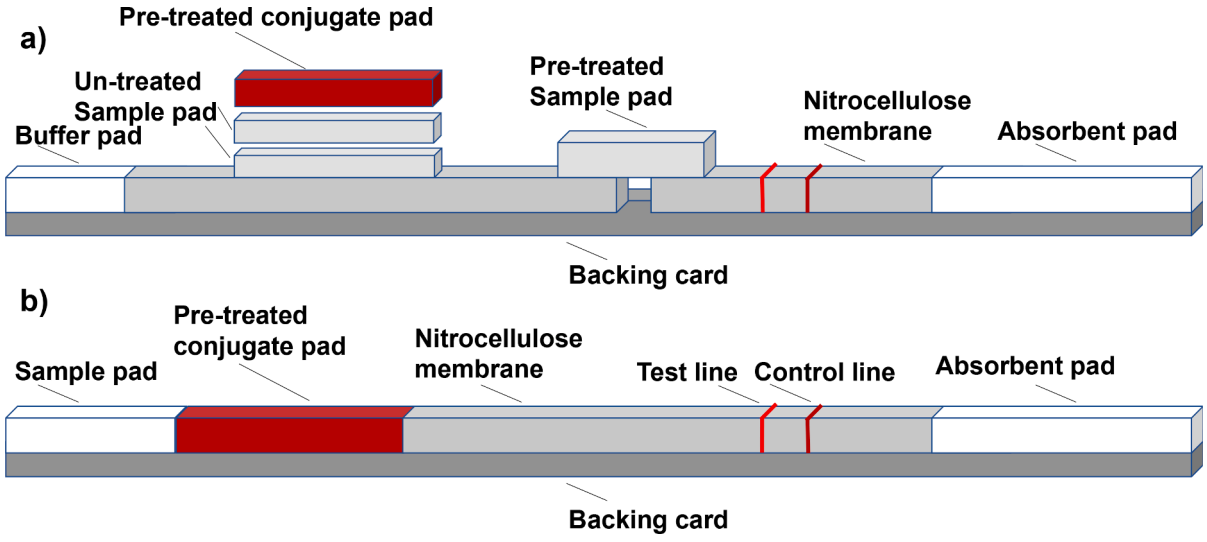

Fig. 1. Assembly of LFIA strips. (a) Bridged structure with sample pad residing on the 3-mm gap; (b) Conventional LFIA consists of a sample pad, conjugate pad, NC membrane, and absorbent pad.

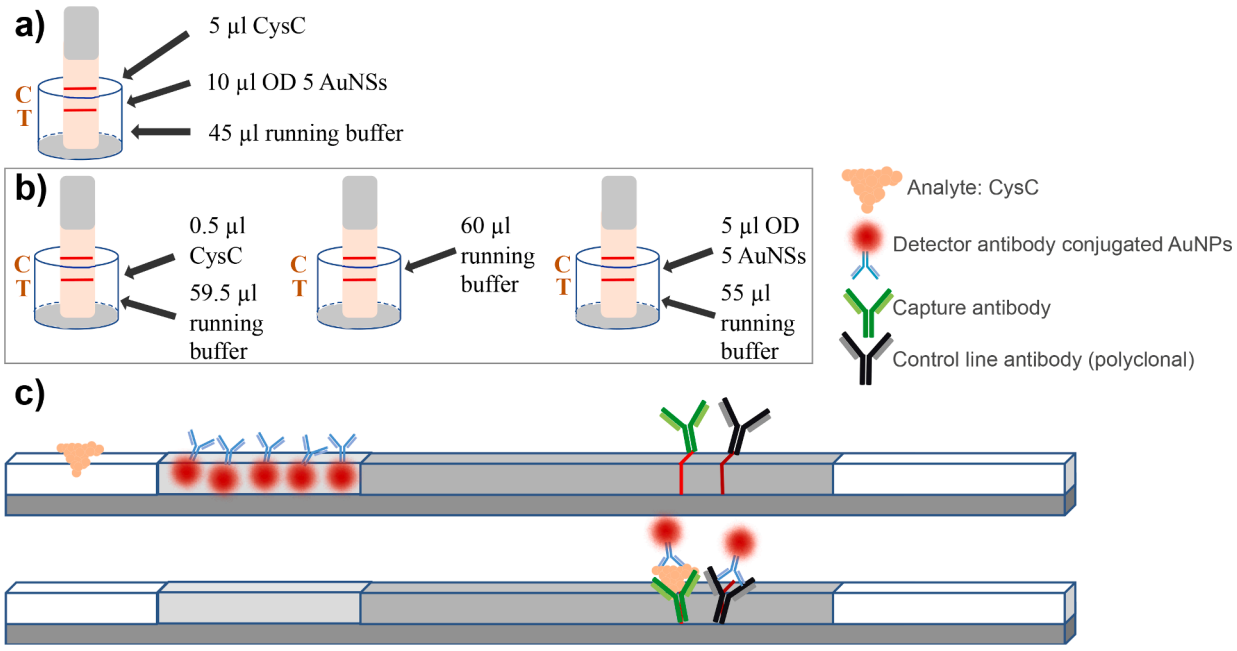

Fig. 2. (a) Conventional LFIA with sum volume of analyte (CysC), AuNSs, and running buffer as 60 µl (dipstick format); (b) LFIAs with wash-step: CysC being added in followed by a wash step before adding mAbs conjugated AuNSs [41] (dipstick format); (c) Conventional LFIAs mechanism, with mAbs conjugated AuNPs being immobilized on the pre-treated conjugate pad and capture Ab and control line Ab being immobilized on the NC membrane separately. After CysC was added to the sample pad, the running buffer was added to the sample pad and it would flush the CysC bound mAbs AuNPs conjugates to the test line and control line region. The test line capture Ab would capture the compound thus indicating a red-colored line. Control line Ab would bind the detector mAbs conjugated on AuNPs with the absence of CysC.

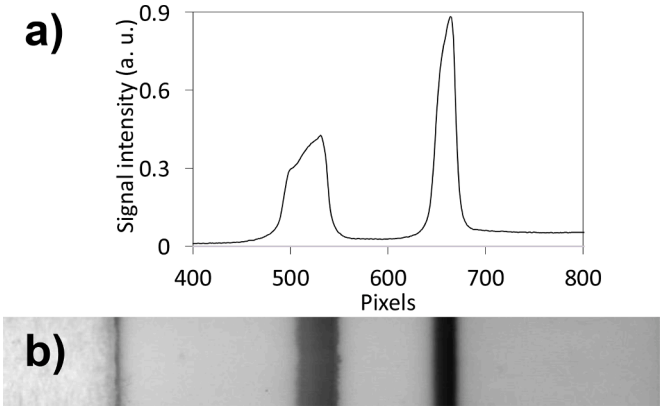

Fig. 3. (a) An example of a scanned LFIA strip via Lumos reader. (b) mAbs conjugated AuNPs in the detection of 5 mg/L CysC with CN 95 NC membrane. Sample volume: 10 µl, with 5 µl OD 5 AuNPs conjugate and 45 µl running buffer (10 mM PBS + 0.1% Tween + 1% BSA).

shows the optimal LFIAs performance among all (Fig. 4(a) (b)). Notwithstanding, 537 µg/ml mAbs bound AuNRs' conjugate exerts a maximum absorbance (Fig. 4(c)), but the idealized LFIAs performance was reached with binding mAbs' concentration at 45 µg/ml, Fig. 4(d).

It is challenging to determine the optimum mAbs concentration with UV-vis spectra only. Thus, DLS was deployed to evaluate the conjugation of AuNSs and biomolecules. DLS had been proved as an effective and appropriate method for investigating the conjugation reaction of AuNPs [43]. R_h of AuNPs increases from 80.2 n ± 1.0 nm (25 µg/ml mAbs) and peaks at 125.9 ± 11.6 nm (mAbs concentration 1074 µg/ml), Fig. 5(a). The excessive addition of the mAbs after 1074 µg/ml indicates the agglomeration (mAbs concentrations 1253, 1432, and 1611 µg/ml. This is following research suggesting that less mAbs binding still guarantees the LFIAs performance [44]. However, LFIAs sensitivity in the detection of CysC with AuNPs peaks when mAbs concentration is 358 µg/ml, Fig. 5 (b). This is following the results of UV-vis, Fig. 4(a) (b). Meanwhile, DLS analyses were carried out for hydrodynamic radius measurements of AuNRs [45]. R_h of mAbs – AuNRs increases from 36.3 nm ± 3.0 nm (15 µg/ml mAbs) and peaks at 55.9 ± 4.5 nm (895 µg/ml mAbs), Fig. 5(c), with Fig. 5(d) shows optimum colorimetric signal intensity with AuNRs as 0.49 at a mAbs concentration of 45 µg/ml.

The maximum R_h is inequivalent to optimum LFIAs sensitivity. As maximum R_h of AuNPs conjugate is 125.9 ± 11.6 nm (1074 µg/ml conjugated mAbs) but LFIAs sensitivity peaks when conjugated mAbs concentration is 358 µg/ml. This is in accordance with the results from Fig. 4(a) (b), which are AuNPs UV-vis spectra and LFIAs. Similarly, 895 µg/ml mAbs – AuNRs conjugate has maximum R_h as 55.9 ± 4.5 nm, Fig. 5(c), but Fig. 5(d) shows 45 µg/ml AuNRs conjugate displaying optimal assay line intensity in detecting 0.5 mg/L CysC. This is also in accordance with the research findings stating the optimized antibody amount for LFIAs can be smaller than the amount generating the maximum particle R_h [44].

3.2. *The tradeoff between detection limit and detection range*

Hook effects are universally observed in colorimetric LFIAs development [46]. Fig. 4(d) shows the hook effects of CysC detected with the AuNRs. With CysC concentration increasing from 2.5 to 5 mg/L, a decrease is observed with the test line signal intensities mildly dropping from 0.991 to 0.907. With hook effects of CysC immunoassay being reported [47,48], these challenges the quantifications of CysC as a higher concentration of the analyte might correspond to an acceptable value thus failing to alarm the patients of the early renal malfunction. Notwithstanding, AuNPs' test line signal intensities of 2.5 mg/L, 4 mg/L, and 5 mg/L CysC are visually identical, Fig. 6(a). The same trend was observed in AuNRs conjugates, with 2.5 mg/L, 4 mg/L, and 5 mg/L analytes CysC having assay line signal intensities of 0.25, 0.26, and 0.26, respectively. To obtain a wider detection range while maintaining the clinical detection limit, a step-wash before the release of AuNSs was

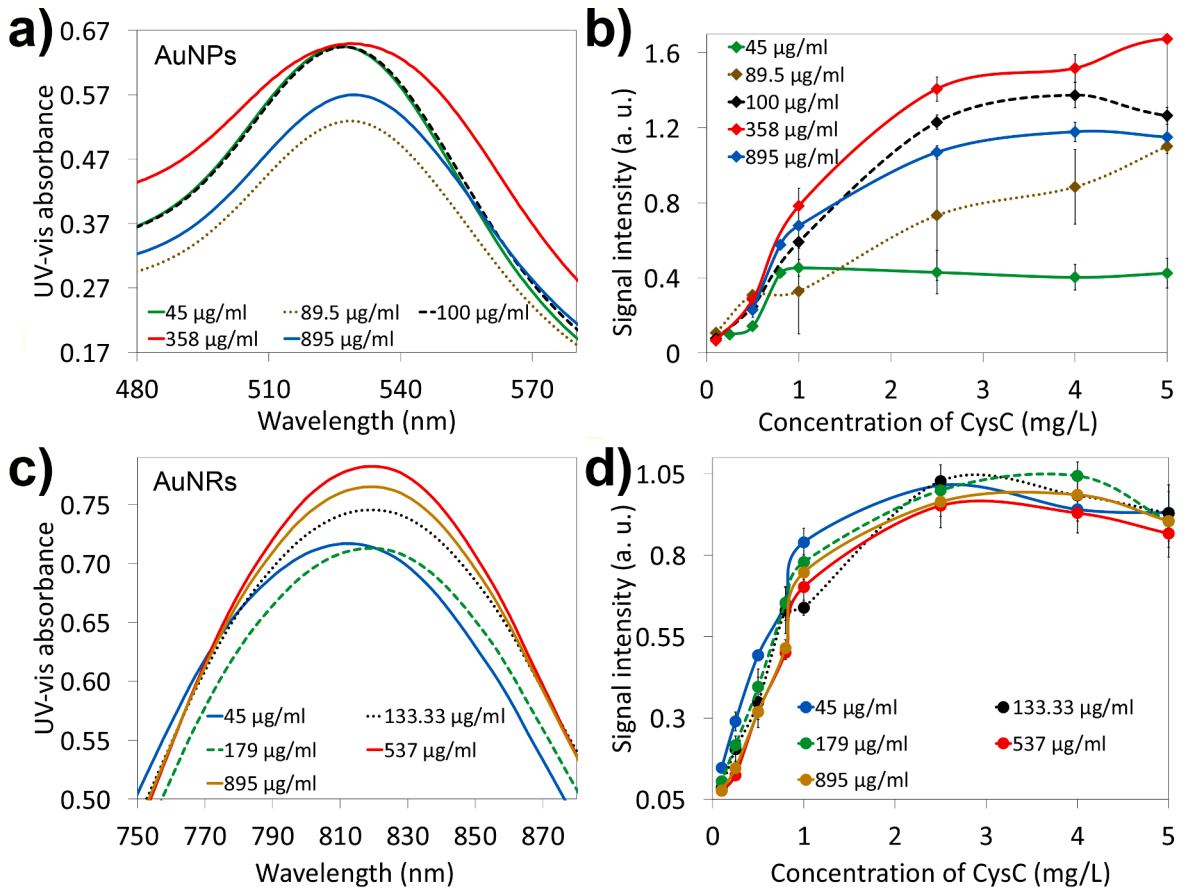

Fig. 4. (a) UV-vis spectra of multiple mAbs – AuNPs (OD 10) measured in a 0.1 cm path length cuvette, with concentrations of mAbs conjugated with AuNPs between 45 μg/ml and 895 μg/ml; (b) LFIA of AuNPs (OD 10) with CysC concentration from 0.1 mg/L to 5 mg/L; (c) AuNRs mAbs conjugates (OD 15) UV-vis spectra measured in a 0.1 cm path length cuvette, with mAbs concentrations ranging from 45 to 895 μg/ml; (d) LFIAs of correspondent AuNRs conjugates (OD 15), CysC: 0.1–5 mg/L.

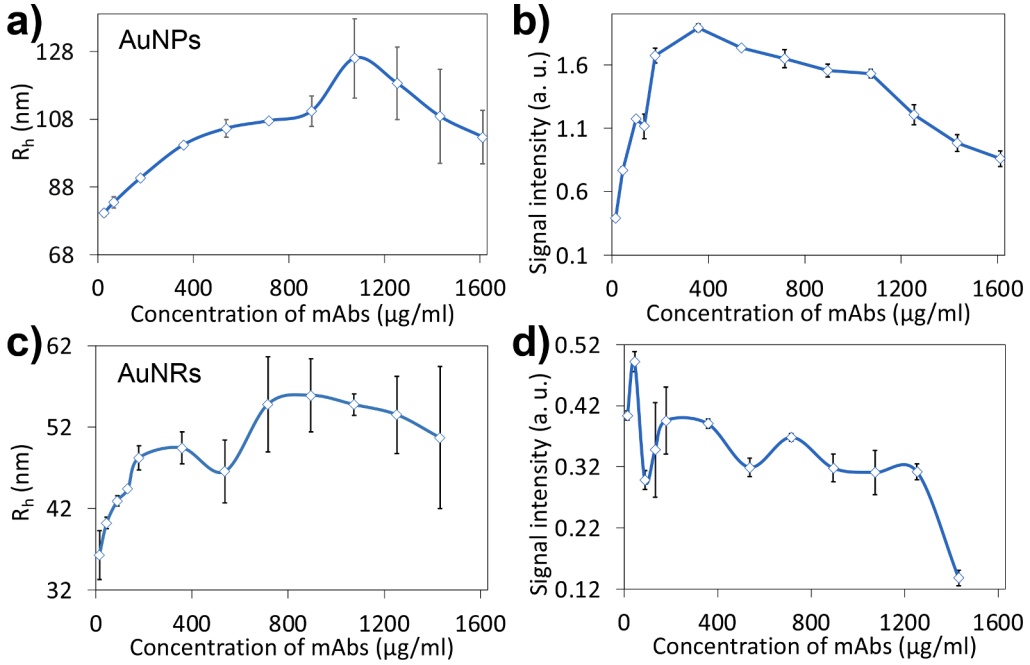

Fig. 5. (a) mAbs conjugated AuNPs' hydrodynamic diameters with increase of mAbs' concentration; (b) LFIAs of AuNPs conjugates in OD 10 with CysC concentration as 2 mg/L; (c) hydrodynamic size of mAbs AuNRs conjugates in different bound mAbs concentrations; (d) LFIAs of AuNRs conjugates in OD 15, with CysC as 0.5 mg/L.

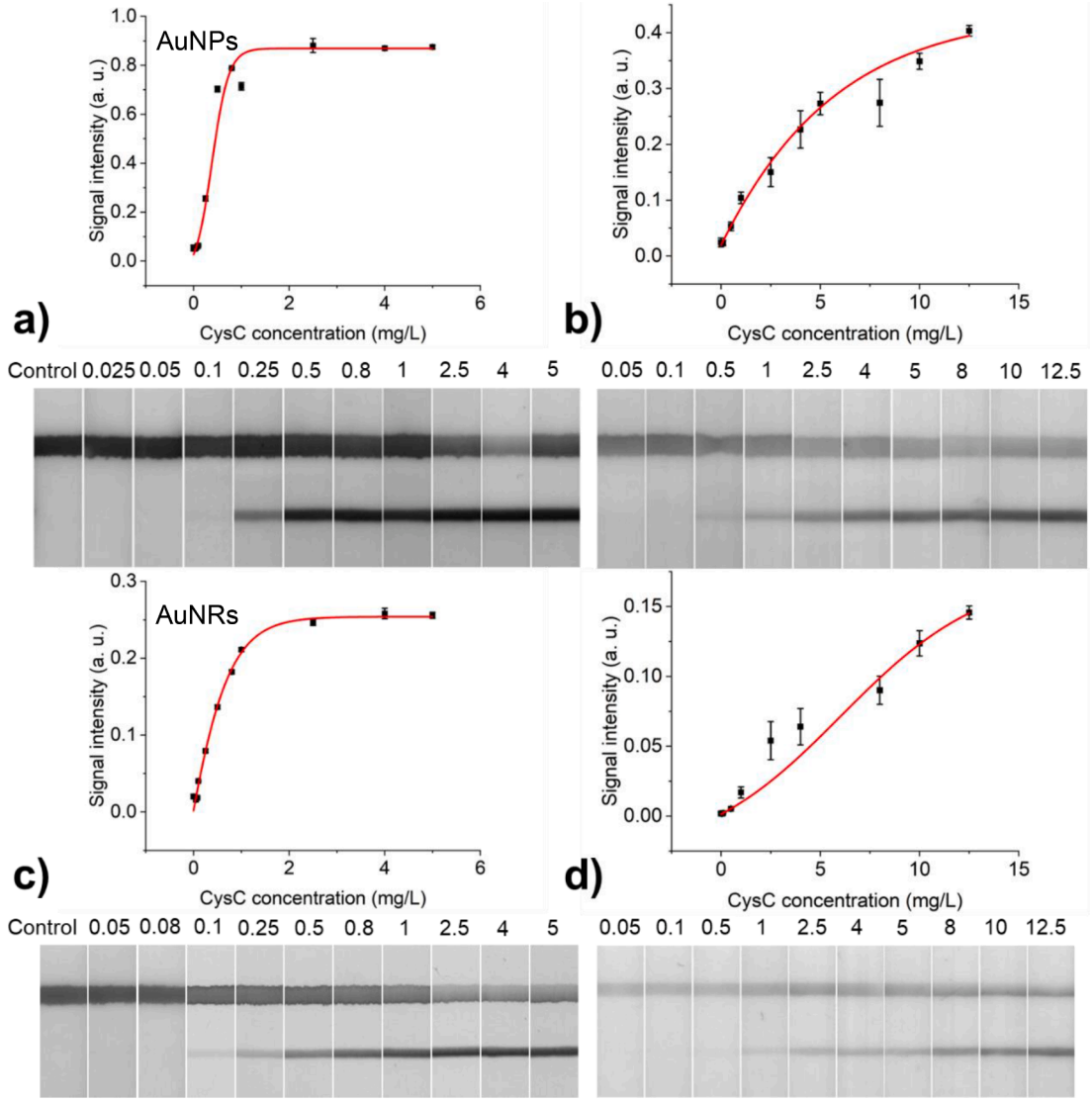

Fig. 6. (a) AuNPs in 358 μg/ml mAbs for CysC detection from 0.1 to 5 mg/L, with dipstick assay format; (b) AuNPs in step-wash format for detection of CysC from 0.05 to 12.5 mg/L; (c) AuNRs in 45 μg/ml mAbs plots of colorimetric signal intensity against CysC concentrations in the dipstick LFIAs format, CysC concentration: 0.1– 5 mg/L; (d) AuNRs with a wash step in between the analyte and release of mAbs bounded AuNSs conjugates [37], CysC concetration: 0.05– 12.5 mg/L. All assay format: dipstick with running buffer components: 10 mM PBS + 0.1% Tween + 1% BSA.

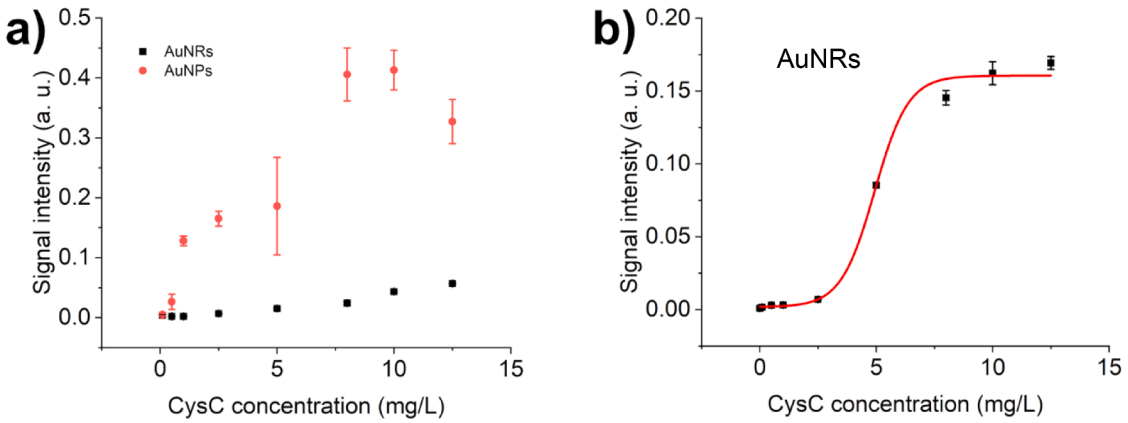

Fig. 7. (a) AuNPs and AuNRs conjugates' colorimetric test lines signal intensities, CysC concentration: 0.1– 12.5 mg/L, sample dilution in 1: 50; (b) AuNRs conjugate with standard LFIAs dipstick format, with sample diluted in 1: 10 ratio. 2.5 μl sample volume with 5 μl OD 5 and 52.5 μl running buffer (10 mM PBS + 0.1% Tween + 1% BSA).

conducted, with detection ranges up to 12.5 mg/L CysC, Fig. 6(b) and (d). Fig. 6(b) (d) utilize the 1% BSA in running buffer whilst 2% BSA running buffer generates non-specific binding in mAbs – AuNRs LFIAs, summarised in the supporting information Fig. S1. The wash step enables the wash-off of the unbound analyte CysC molecules from the test line, freeing up the space for mAbs – AuNSs conjugate to bind analyte immobilized by capture antibody at the test line region.

To certify the test line intestines of mAbs – AuNPs conjugates and mAbs – AuNRs conjugates, analyte CysC were diluted 50-fold in PBS, with test line intensities of mAbs – AuNPs conjugates (black line) and mAbs – AuNRs conjugates (red line) shown in Fig. 7(a). With the general signal intensity values of AuNPs conjugates above AuNRs conjugates, Fig. 7(a) suggests AuNP conjugates have a more intensified line signal compared with AuNRs conjugates. However, AuNRs conjugates are more sensitive in the detection of CysC as mAbs needed to reach the clinical range of CysC detection is 45 μg/ml for AuNRs, Figs. 4(b) 5(d) 6 (d). AuNRs sensitivity in the detection of CysC is better than AuNPs potentially due to the redshift towards the long wavelength so that the extinction coefficient of AuNRs increases [49]. However, because the maximum absorbance of AuNRs is in the near-infrared region (>700 nm), which increases the difficulty for visual reading out thus leading to the visual signal test line intensities weaker than AuNPs' [50]. Besides having stronger and more flexible near-infrared region absorption, the anisotropic AuNRs have better sensitivity than AuNPs potentially due to their larger surface area [51]. Though both AuNRs and AuNPs become unstable with the increasing concentration of salt, AuNRs' two different longitudinal and transverse resonance plasmon absorption bands [52] provide the potential for application in biosensing [53]. AuNRs are not only more sensitive in the detection of biomolecules, with C-reactive protein as an example [50], but they are also more sensitive to the local environment [54] in the detection of heavy metals [55].

To enable the wash-step with single solution adding instead of multi-step solution addition, the bridged structure is introduced to realize the delayed release of the mAbs – AuNSs conjugates. Buffer from the buffer pad would encounter the hindrance of the intermediate pad before reaching the mAbs – AuNSs conjugates on top of the intermediate pad. This would facilitate the controlled release of the mAbs – AuNSs after the sample reaches the test line region. Wash-step with three stages of reagents addition could be alleviated by bridged structure with only one procedure of fluid addition. With the application of the bridged structure in Fig. 8, mAbs – AuNPs conjugate could detect CysC within its clinical range with a sample dilution factor of 1:1.5 in PBS. Nevertheless, AuNRs conjugates in Fig. 7(b) can linearly detect CysC with samples diluted in PBS with a 1:10 dilution factor. With sample dilution, the linear detection range is extended (Fig. 7(b)) compared with Fig. 6(c), whilst keeping the sample volume as 2.5 μl, which is easy to pipette. Due to the multi-wash step of dipstick assay format and complicated LF components assembling of the bridged structure, the complete LFIAs in the conventional structure were assembled with a results turnaround time of 10 min. 2.5 μl sample volume is required with no wash step involved. Comparison is shown via AuNPs with wash-step and 0.5 μl CysC (Fig. 6 (b)), AuNPs bridged-structure (Fig. 8), and conventional LFIAs structure with 2.5 μl sample volume (Fig. 9).

The detection limit of this study is calculated by LoD (limit of detection) = mean $_{blank}$ + 3 × σ $_{blank}$[56,57]. Sigmoidal curve fitting with the dose-response function was selected, Fig. 6(a) (b) showing AuNPs conventional and step-wash dipstick assay have the LoD as 0.1 and 0.42 mg/L separately, see supporting information Tables S1, S2. Similarly, Fig. 6(c) (d) shows AuNRs conventional and step-wash LFIA in dipstick format with LoD as 0.08 mg/L and 0.35 mg/L, respectively, see supporting information Tables S3, S4. Nevertheless, AuNRs in 10-fold sample dilution have the LoD of 0.49 mg/L, see supporting information Table S5, with the bridged structure having the LoD of 0.87 mg/L, see supporting information Table S6. The summary of LFIAs LoD and correspondent R^2 can be found in the supporting information Table S9.

Notably, Fig. 4(b) suggests the 89.5 μg/ml mAbs in AuNPs binding has a linear increase in detection of CysC. Thus, the comparison of 89.5 μg/ml and 358 μg/ml AuNPs' mAbs binding concentrations in the detection of CysC in PBS is evaluated, Fig. 9(b). The LoD of 89.5 μg/ml AuNPs conjugates is 1.04 mg/L, see supporting information in Table S7. LoD of 358 μg/ml mAbs – AuNPs is 0.95 mg/L, see supporting information in Table S8. In this regard, higher mAbs binding concentration will avail the detection limit. But with normal CysC value stays between 0.57 and 1.03 mg/L for females, and from 0.70 to 1.10 mg/L for males [3], 89.5 μg/ml mAbs binding concentration is favoured. Additionally, serum CysC level for stage 1 and 2 chronic kidney disease is 1.34 mg/L, above the reference level of 1.09 mg/L [21]. The linear range for the 89.5 μg/ml AuNPs is 3.69 to 6.37 mg/L with 358 μg/ml AuNPs' linear range between 3.93 and 6.10 mg/L correspondently. The calculation is conducted according to linear range calculation in the sigmoidal curve [58,59]. This further suggests that 89.5 μg/ml mAbs concentration for AuNPs conjugation is favoured for quantification of the CysC level, other than 358 μg/ml as a wider linear range is provided by 89.5 μg/ml AuNPs.

To address the reproducibility of the LFIAs, we performed the intra- and inter- assay comparison. 3 batches of CysC lyophilized powder being spiked in PBS were performed with AuNPs' mAbs concentration at 89.5 μg/ml, Fig. 9(a). Intra- assay comparisons were addressed via the coefficient of variation (CV%) by averaging the CV% of duplicate reportable results from the individual assay. Meanwhile, inter- assay comparison is averaging the CV% of 3 batches' duplicate reportable results [60], with intra- assay CV% as 13.69% and inter- assay CV% as 21.75%

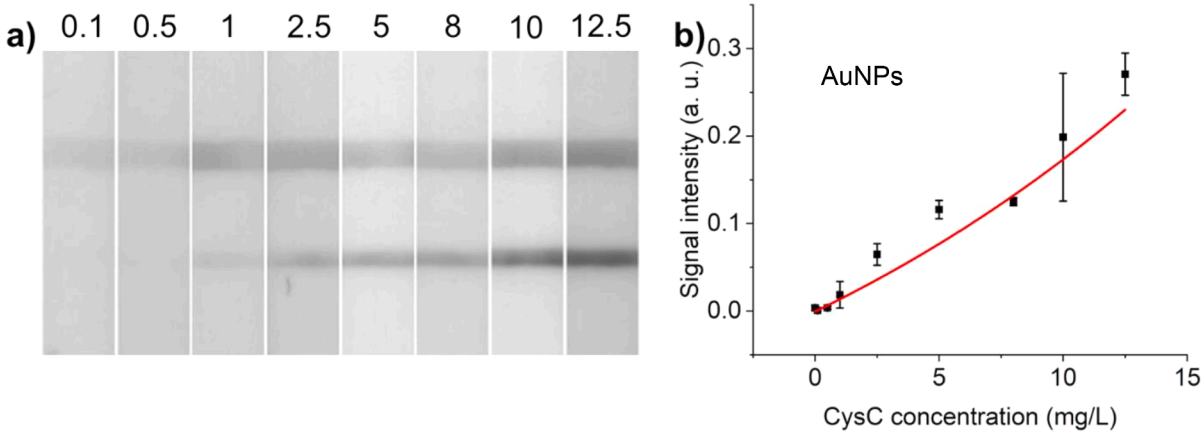

Fig. 8. (a) The bridged structure for LFIAs with AuNPs conjugate, CysC: 0.1– 12.5 mg/L; (b) Correspondent colorimetric line intensities plotting against CysC concentrations.

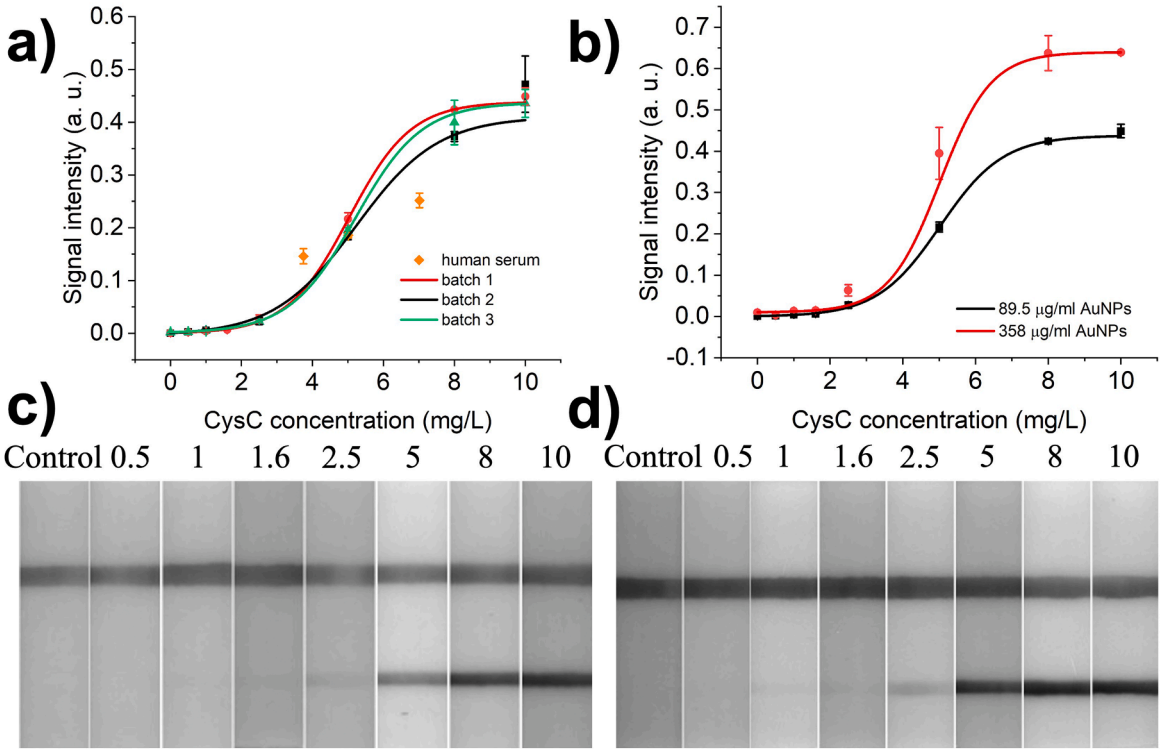

Fig. 9. (a) Intra- and inter- assay comparison, with lyophilised CysC being spiked in PBS matrix, CysC: 0.5– 10 mg/L. Together with human serum samples diluted in 36-fold to address the matrix effect; (b) Comparison of mAbs concentration at 89.5 and 358 μg/ml for AuNPs conjugation, CysC used were in PBS matrix, from 0.5 to 10 mg/L; (c) Correspondent LFIAs strips colorimetric line intensities with CysC concentrations accordingly when mAbs concentration is at 89.5 μg/ml and (d) 358 μg/ml.

accordingly. We have also tested human samples with known CysC values provided by the local Health and Social Care trust. The matrix effect is still a critical issue in biosensor development [61], as the complexity of the matrix containing multiple nonspecific proteins and other components would hinder the recognition of the target protein [62]. Here, with the 36-fold dilution of the human serum sample in the PBS medium, the matrix effect was evaluated via recovery rate, see Table. 1. Matrix effect had been addressed in the previous work accordingly. The magnetic nanoparticles increased tropomyosin detection performance by mitigating the matrix effect [63]. Similarly, the up-converting phosphors having little background influence caused by complex matrices make it a candidate for sample detection in various matrices [64].

Table 1
Recovery rate of human samples CysC level quantification in PBS medium, with human samples diluted 36-fold in PBS medium. LFIAs result in the recovery rate and coefficient of variation.

Human serum sample (mg/L)	Measured concentration (mg/L)	Recovery (%)	CV (%)
7.02	5.52 ± 0.13	80.33 ± 2.02	3.52
5.01	4.91 ± 0.05	98.02 ± 0.94	2.80
3.75	4.52 ± 0.15	119.77 ± 3.72	2.11
Average		99.37 ± 2.23	2.81

4. Conclusion

We developed the LFIAs by contrasting two AuNSs conjugates: AuNPs and AuNRs conjugates and report the use of AuNPs and AuNRs conjugates in CysC clinical level evaluation. Both AuNRs and AuNPs reveal their potential in colorimetric LFIAs in the detection of CysC. Even with test line signal intensities of AuNPs generally greater than AuNRs' (Fig. 7(a)), AuNRs conjugates are more sensitive as a smaller amount of mAbs (45 μg/ml) is required to detect CysC within its clinical range with a lower LoD than AuNPs. With wash-step in between the analyte and release of the conjugates, together with the bridged structure LFIAs, the detection range was extended. Due to the longer turnaround time of the wash-step LFIAs and the complex assembling of bridged structure LFIAs, the conventional LFIAs format is assembled with AuNPs' mAbs binding concentration at 89.5 μg/ml. This suffices the detection requirements of CysC in both PBS medium and serum. Collectively, this work (1) develops colorimetric LFIAs for CysC detection within its clinical range, reducing the workload of healthcare professionals and increasing home-based disease monitoring; (2) reduces the excessive amounts of mAbs used in the conjugation process and guides the future LFIAs development, (3) optimized the detection range whilst maintaining the detection sensitivity, which is a trade-off commonly existing in the LFIAs development and evaluated the human serum samples CysC with results turnaround time shortened as 10 min. Future work will be focusing on the application of developed LFIAs for CysC in clinical use through a preliminary clinical trial with human serum. Multianalytes with other cardio and renal biomarkers would increase the precision of disease detection and could be a potential diagnostic reference for healthcare professionals.

Declaration of Competing Interest

The authors declare that they have no known competing financial interests or personal relationships that could have appeared to influence the work reported in this paper.

Acknowledgments

This research is conducted under the project of Eastern Corridor Medical Engineering Centre (ECME) and funded by the European

Union's INTERREG VA program (Grant ID: IVA5034), managed by the Special EU Programs Body (SEUPB).

Supplementary materials

Supplementary material associated with this article can be found, in the online version, at doi:10.1016/j.snr.2022.100121.

References

[1] P. Di Nicolò, The dark side of the kidney in cardio-renal syndrome: renal venous hypertension and congestive kidney failure, Heart Fail. Rev. (2018) 291–302, https://doi.org/10.1007/s10741-018-9673-4. Heart Failure Reviews.

[2] J. Helmersson-Karlqvist, M. Lipcsey, J. Ärnlöv, M. Bell, B. Ravn, A. Dardashti, A. Larsson, Cystatin C predicts long term mortality better than creatinine in a nationwide study of intensive care patients, Sci. Rep. 11 (1) (2021) 1–9, https://doi.org/10.1038/s41598-021-85370-8.

[3] B.E. Edinga-Melenge, A.T. Yakam, J.R. Nansseu, C. Bilong, S. Belinga, E. Minkala, P.A. Noudjeu, M. Ondhoua, S.W. Kokola, V.J. Ama Moor, G Ashuntantang, Reference intervals for serum cystatin c and serum creatinine in an adult Sub-Saharan African population, BMC Clin. Pathol. 19 (1) (2019) 1–9, https://doi.org/10.1186/s12907-019-0086-7.

[4] Z. Yong, X. Pei, B. Zhu, H. Yuan, W. Zhao, Predictive value of serum Cystatin C for acute kidney injury in adults: a meta-analysis of prospective cohort trials, Sci. Rep. 7 (2017) 1–11, https://doi.org/10.1038/srep41012. January.

[5] Y. Wang, W. Li, J. Yang, M. Zhang, C. Tian, M. Ma, Q. Zhang, Association between Cystatin C and the risk of ischemic stroke: a systematic review and meta-analysis, J. Mol. Neurosci. 69 (3) (2019) 444–449, https://doi.org/10.1007/s12031-019-01373-1.

[6] T. Kobayashi, H. Yokokawa, K. Fujibayashi, T. Haniu, T. Hisaoka, H. Fukuda, T. Naito, Association between high Cystatin C levels and carotid atherosclerosis, World J. Cardiol. 9 (2) (2017) 174, https://doi.org/10.4330/wjc.v9.i2.174.

[7] A.S. Bargnoux, L. Piéroni, J.P. Cristol, N. Kuster, P. Delanaye, M.C. Carlier, S. Fellahi, A. Boutten, C. Lombard, A. González-Antuña, V. Delatour, E Cavalier, Multicenter evaluation of Cystatin C measurement after assay standardization, Clin. Chem. 63 (4) (2017) 833–841, https://doi.org/10.1373/clinchem.2016.264325.

[8] K.S.S. Devi, U.M. Krishnan, Microfluidic electrochemical immunosensor for the determination of Cystatin C in human serum, Microchim. Acta (10) (2020) 187, https://doi.org/10.1007/s00604-020-04503-4.

[9] S. Natarajan, M. Derosa, J. Joseph, M.I. Shah, S. Karthik, Aptamer based lateral flow assays for rapid and sensitive detection of CKD marker Cystatin, C (2021) 1–5, https://doi.org/10.1109/memea52024.2021.9478684.

[10] K. Shah, P. Maghsoudlou, Enzyme-linked immunosorbent assay (ELISA): the basics, Br. J. Hosp. Med. 77 (7) (2016) C98–C101, https://doi.org/10.12968/hmed.2016.77.7.c98.

[11] E.K.G. Trindade, B.V.M. Silva, R.F Dutra, A Probeless and label-free electrochemical immunosensor for Cystatin C detection based on ferrocene functionalized-graphene platform, Biosens. Bioelectron. 138 (2019), 111311, https://doi.org/10.1016/j.bios.2019.05.016. February.

[12] S. Natarajan, M.C. Derosa, M.I. Shah, J. Jayaraj, Development and evaluation of a quantitative fluorescent lateral flow immunoassay for Cystatin-C, a renal dysfunction biomarker, Sensors (9) (2021) 21, https://doi.org/10.3390/s21093178.

[13] L. Huang, J. Jin, L. Ao, C. Jiang, Y. Zhang, H.M. Wen, J. Wang, H. Wang, J. Hu, Hierarchical plasmonic-fluorescent labels for highly sensitive lateral flow immunoassay with flexible dual-modal switching, ACS Appl. Mater. Interfaces 12 (52) (2020) 58149–58160, https://doi.org/10.1021/acsami.0c18667.

[14] J. Hu, Y.Z. Jiang, M. Tang, L.L. Wu, H.Y. Xie, Z.L. Zhang, D.W Pang, Colorimetric-fluorescent-magnetic nanosphere-based multimodal assay platform for salmonella detection, Anal. Chem. 91 (1) (2019) 1178–1184, https://doi.org/10.1021/acs.analchem.8b05154.

[15] X. Chen, L. Ding, X. Huang, Y. Xiong, Tailoring noble metal nanoparticle designs to enable sensitive lateral flow immunoassay, Theranostics 12 (2) (2022) 574–602, https://doi.org/10.7150/thno.67184.

[16] X. Gao, J. Boryczka, P. Zheng, S. Kasani, F. Yang, E.B. Engler-Chiurazzi, J. W. Simpkins, J.G. Wigginton, N. Wu, A "hot spot"-enhanced paper lateral flow assay for ultrasensitive detection of traumatic brain injury biomarker S-100β in blood plasma, Biosens. Bioelectron. 177 (2021), 112967, https://doi.org/10.1016/j.bios.2021.112967. November 2020.

[17] S.K. Bikkarolla, S.E. McNamee, P. Vance, J. McLaughlin, High-sensitive detection and quantitative analysis of thyroid-stimulating hormone using gold-nanoshell-based lateral flow immunoassay device, Biosensors (3) (2022) 12, https://doi.org/10.3390/bios12030182.

[18] Y. Zhou, Y. Chen, Y. Liu, H. Fang, X. Huang, Y. Leng, Z. Liu, L. Hou, W. Zhang, W. Lai, Y. Xiong, Controlled copper *in situ* growth-amplified lateral flow sensors for sensitive, reliable, and field-deployable infectious disease diagnostics, Biosens. Bioelectron. 171 (2021), 112753, https://doi.org/10.1016/j.bios.2020.112753. October 2020.

[19] L. Su, L. Wang, J. Xu, Z. Wang, X. Yao, J. Sun, J. Wang, D. Zhang, Competitive lateral flow immunoassay relying on Au-SiO_2 Janus nanoparticles with an asymmetric structure and function for furazolidone residue monitoring, J. Agric. Food Chem. 69 (1) (2021) 511–519, https://doi.org/10.1021/acs.jafc.0c06016.

[20] Z. Gao, H. Ye, Q. Wang, M.J. Kim, D. Tang, Z. Xi, Z. Wei, S. Shao, X. Xia, Template regeneration in galvanic replacement: a route to highly diverse hollow nanostructures, ACS Nano 14 (1) (2020) 791–801, https://doi.org/10.1021/acsnano.9b07781.

[21] J. Dsa, S. Shetty, R.R. Bhandary, A.V Rao, Association between serum Cystatin C and creatinine in chronic kidney disease subjects attending a tertiary health care centre, J. Clin. Diagn. Res. 11 (4) (2017) BC09–BC12, https://doi.org/10.7860/JCDR/2017/26655.9655.

[22] S. Shrivastava, T.Q. Trung, N.E. Lee, Recent progress, challenges, and prospects of fully integrated mobile and wearable point-of-care testing systems for self-testing, Chem. Soc. Rev. 49 (6) (2020) 1812–1866, https://doi.org/10.1039/c9cs00319c.

[23] V. Shirshahi, G. Liu, Enhancing the analytical performance of paper lateral flow assays: from chemistry to engineering, TrAC Trends Anal. Chem. 136 (2021), 116200, https://doi.org/10.1016/j.trac.2021.116200.

[24] J. Wang, C. Jiang, J. Jin, L. Huang, W. Yu, B. Su, J. Hu, Ratiometric fluorescent lateral flow immunoassay for point-of-care testing of acute myocardial infarction, Angew. Chem. 133 (23) (2021) 13152–13159, https://doi.org/10.1002/ange.202103458.

[25] B. Zhang, X. Yang, X. Liu, J. Li, C. Wang, S. Wang, Polyethyleneimine-interlayered silica-core quantum dot-shell nanocomposites for sensitive detection of: Salmonella Typhimurium via a lateral flow immunoassay, RSC Adv. 10 (5) (2020) 2483–2489, https://doi.org/10.1039/c9ra09252h.

[26] N. Cheng, Y. Song, Q. Shi, D. Du, D. Liu, Y. Luo, W. Xu, Y. Lin, Au@Pd nanopopcorn and aptamer nanoflower assisted lateral flow strip for thermal detection of exosomes, Anal. Chem. 91 (21) (2019) 13986–13993, https://doi.org/10.1021/acs.analchem.9b03562.

[27] L. Huang, L. Ding, J. Zhou, S. Chen, F. Chen, C. Zhao, J. Xu, W. Hu, J. Ji, H. Xu, G. L. Liu, One-step rapid quantification of SARS-CoV-2 virus particles via low-cost nanoplasmonic sensors in generic microplate reader and point-of-care device, Biosens. Bioelectron. 171 (2021), 112685, https://doi.org/10.1016/j.bios.2020.112685. October 2020.

[28] C. Huang, T. Wen, F.J. Shi, X.Y. Zeng, Y.J. Jiao, Rapid detection of IgM antibodies against the SARS-CoV-2 virus via colloidal gold nanoparticle-based lateral-flow assay, ACS Omega 5 (21) (2020) 12550–12556, https://doi.org/10.1021/acsomega.0c01554.

[29] S. Aoyama, Y. Akiyama, K. Monden, M. Yamada, M. Seki, Thermally imprinted microcone structure-assisted lateral-flow immunoassay platforms for detecting disease marker proteins, Analyst 144 (5) (2019) 1519–1526, https://doi.org/10.1039/c8an01903g.

[30] C. Wang, W. Shen, Z. Rong, X. Liu, B. Gu, R. Xiao, S. Wang, Layer-by-layer assembly of magnetic-core dual quantum dot-shell nanocomposites for fluorescence lateral flow detection of bacteria, Nanoscale 12 (2) (2020) 795–807, https://doi.org/10.1039/c9nr08509b.

[31] T. Lee, J.H. Ahn, J. Choi, Y. Lee, J.M. Kim, C. Park, H. Jang, T.H. Kim, M.H. Lee, Development of the troponin detection system based on the nanostructure, Micromachines (3) (2019) 10, https://doi.org/10.3390/mi10030203.

[32] T. Bai, M. Wang, M. Cao, J. Zhang, K. Zhang, P. Zhou, Z. Liu, Y. Liu, Z. Guo, X Lu, Functionalized Au@Ag-Au nanoparticles as an optical and SERS dual probe for lateral flow sensing, Anal. Bioanal. Chem. 410 (9) (2018) 2291–2303, https://doi.org/10.1007/s00216-018-0850-z.

[33] E.G. Rey, D. O'Dell, S. Mehta, D Erickson, Mitigating the hook effect in lateral flow sandwich immunoassays using real-time reaction kinetics, Anal. Chem. 89 (9) (2017) 5095–5100, https://doi.org/10.1021/acs.analchem.7b00638.

[34] L.E.M. Miles, D.A. Lipschitz, C.P. Bieber, J.D. Cook, Measurement of serum ferritin by a 2-site immunoradiometric assay, Anal. Biochem. 61 (1) (1974) 209–224, https://doi.org/10.1016/0003-2697(74)90347-9.

[35] J. Tate, G. Ward, Interferences in immunoassay, Clin. Biochem. Rev. 25 (2) (2004) 105–120. PMID: 18458713; PMCID: PMC1904417.

[36] Anthony W.B., Dilution protocols for detection of hook effects/prozone phenomenon, Clin. Chem., Volume 46, Issue 10, 1 October 2000, Pages 1719–1720, 10.1093/clinchem/46.10.1719.

[37] J. Oh, H.A. Joung, H.S. Han, J.K. Kim, M.G. Kim, A hook effect-free immunochromatographic assay (HEF-ICA) for measuring the C-reactive protein concentration in one drop of human serum, Theranostics 8 (12) (2018) 3189–3197, https://doi.org/10.7150/thno.24034.

[38] G. He, T. Dong, Z. Yang, Z. Jiang, Mitigating hook effect in one-step quantitative sandwich lateral flow assay by timed conjugate release, Talanta 240 (2022), 123157, https://doi.org/10.1016/j.talanta.2021.123157. December 2021.

[39] A. Srisrattakarn, P. Tippayawat, A. Chanawong, R. Tavichakorntrakool, J. Daduang, L. Wonglakorn, A. Lulitanond, Development of a prototype lateral flow immunoassay for rapid detection of staphylococcal protein a in positive blood culture samples, Diagnostics (10) (2020) 10, https://doi.org/10.3390/diagnostics10100794.

[40] G.M.S. Ross, G.I. Salentijn, M.W.F.A Nielen, Critical comparison between flow-through and lateral flow immunoassay formats for visual and smartphone-based multiplex allergen detection, Biosensors 9 (4) (2019), https://doi.org/10.3390/bios9040143.

[41] H. Sadrzadeh, L. Baskin, G. Kline, Variables affecting endocrine tests results, errors prevention and mitigation, in: InEndocrine Biomarkers 1, Elsevier, 2017 Jan, pp. 1–40.

[42] Y. Wang, Y. Ni, Combination of UV–vis spectroscopy and chemometrics to understand protein-nanomaterial conjugate: a case study on human serum albumin and gold nanoparticles, Talanta 119 (2014) 320–330, https://doi.org/10.1016/j.talanta.2013.11.026.

[43] H. Jans, X. Liu, L. Austin, G. Maes, Q Huo, Dynamic light scattering as a powerful tool for gold nanoparticle bioconjugation and biomolecular binding studies, Anal. Chem. 81 (22) (2009) 9425–9432, https://doi.org/10.1021/ac901822w.
[44] N.A. Byzova, I.V. Safenkova, E.S. Slutskaya, A.V. Zherdev, B.B. Dzantiev, Less is more: a comparison of antibody-gold nanoparticle conjugates of different ratios, Bioconjug. Chem. 28 (11) (2017) 2737–2746, https://doi.org/10.1021/acs.bioconjchem.7b00489.
[45] M.A. Hamaly, S.R. Abulateefeh, K.M. Al-Qaoud, A.M. Alkilany, Freeze-drying of monoclonal antibody-conjugated gold nanorods: colloidal stability and biological activity, Int. J. Pharm. 550 (1–2) (2018) 269–277, https://doi.org/10.1016/j.ijpharm.2018.08.045.
[46] X. Hu, J. Wan, X. Peng, H. Zhao, D. Shi, L. Mai, H. Yang, Y. Zhao, X. Yang, Calorimetric lateral flow immunoassay detection platform based on the photothermal effect of gold nanocages with high sensitivity, specificity, and accuracy, Int. J. Nanomed. 14 (2019) 7695–7705, https://doi.org/10.2147/IJN.S218834.
[47] A. Sohrabian, F.H. Noraddin, M. Flodin, A. Fredricsson, A. Larsson, Particle enhanced turbidimetric immunoassay for the determination of urine Cystatin C on Cobas C501, Clin. Biochem. 45 (4–5) (2012) 339–344, https://doi.org/10.1016/j.clinbiochem.2011.12.027.
[48] A.S. Bargnoux, V. Azoury, S. Badiou, K. Klouche, M. Plawecki, N. Kuster, J. P Cristol, Analytical performances of PENIA and PETIA urinary Cystatin C determination allow tubular injury investigation, Ann. Clin. Biochem. 56 (2) (2019) 228–231, https://doi.org/10.1177/0004563218816341.
[49] R.D. Near, S.C. Hayden, R.E. Hunter, D. Thackston, M.A. El-Sayed, Rapid and efficient prediction of optical extinction coefficients for gold nanospheres and gold nanorods, J. Phys. Chem. C 117 (45) (2013) 23950–23955, https://doi.org/10.1021/jp4082596.
[50] F. Scholz, L. Rüttinger, T. Heckmann, L. Freund, A.M. Gad, T. Fischer, A. Gütter, H. H. Söffing, Carboxyl functionalized gold nanorods for sensitive visual detection of biomolecules, Biosens. Bioelectron. (2020) 164, https://doi.org/10.1016/j.bios.2020.112324. May.
[51] Q. Yu, J. Zhang, W. Qiu, K. Li, L. Qian, X. Zhang, G. Liu, Gold nanorods-based lateral flow biosensors for sensitive detection of nucleic acids, Microchim. Acta (4) (2021) 188, https://doi.org/10.1007/s00604-021-04788-z.
[52] J. Wang, H.Z. Zhang, R.S. Li, C.Z. Huang, Localized surface plasmon resonance of gold nanorods and assemblies in the view of biomedical analysis, TrAC Trends Anal. Chem. 80 (2016) 429–443, https://doi.org/10.1016/j.trac.2016.03.015.
[53] C. Xu, L. Lan, Y. Yao, J. Ping, Y. Li, Y. Ying, An unmodified gold nanorods-based DNA colorimetric biosensor with enzyme-free hybridization chain reaction amplification, Sens. Actuators B Chem. 273 (2018) 642–648, https://doi.org/10.1016/j.snb.2018.06.035. January.
[54] Y. Wang, X. Zhou, C. Xu, et al., Gold nanorods as visual sensing platform for chiral recognition with naked eyes, Sci. Rep. 8 (2018) 5296, https://doi.org/10.1038/s41598-018-23674-y.
[55] A. Rajeshwari, D. Karthiga, N. Chandrasekaran, A. Mukherjee, Anti-aggregation-based spectrometric detection of Hg(II) at physiological PH using gold nanorods, Mater. Sci. Eng. C 67 (2016) 711–716, https://doi.org/10.1016/j.msec.2016.05.066.
[56] A.K. Badu-Tawiah, S. Lathwal, K. Kaastrup, M. Al-Sayah, D.C. Christodouleas, B. S. Smith, G.M. Whitesides, H.D. Sikes, Polymerization-based signal amplification for paper-based immunoassays, Lab Chip 15 (3) (2015) 655–659, https://doi.org/10.1039/c4lc01239a.
[57] J.O. Tam, H. de Puig, C.wan Yen, I. Bosch, J. Gómez-Márquez, C. Clavet, K. Hamad-Schifferli, L Gehrke, A comparison of nanoparticle-antibody conjugation strategies in sandwich immunoassays, J. Immunoass. Immunochem. 38 (4) (2017) 355–377, https://doi.org/10.1080/15321819.2016.1269338.
[58] J.L. Sebaugh, P.D. McCray, Defining the linear portion of a sigmoid-shaped curve: bend points, Pharm. Stat. 2 (3) (2003) 167–174, https://doi.org/10.1002/pst.62.
[59] J.L. Sebaugh, Guidelines for accurate EC50/IC50 estimation, Pharm. Stat. 10 (2) (2011) 128–134, https://doi.org/10.1002/pst.426.
[60] H.Y. Hsu, W. Silke, E.M. Schneider, M. Weiss, T.O Joos, Suspension microarrays for the identification of the response patterns in hyperinflammatory diseases, Med. Eng. Phys. 30 (8) (2008) 976–983, https://doi.org/10.1016/j.medengphy.2008.01.003.
[61] I.H. Cho, D.H. Kim, S. Park, Electrochemical biosensors: perspective on functional nanomaterials for on-site analysis, Biomater. Res. 24 (1) (2020) 1–12, https://doi.org/10.1186/s40824-019-0181-y.
[62] A. Angulo-Ibáñez, U. Eletxigerra, X. Lasheras, S. Campuzano, S. Merino, Electrochemical tropomyosin allergen immunosensor for complex food matrix analysis, Anal. Chim. Acta 1079 (2019) 94–102, https://doi.org/10.1016/j.aca.2019.06.030.
[63] M. Aydin, E.B. Aydin, M.K. Sezgintürk, Advances in immunosensor technology, Adv. Clin. Chem. 102 (2021) 1–62, https://doi.org/10.1016/bs.acc.2020.08.001.
[64] Y. Zhao, X. Liu, X. Wang, C. Sun, X. Wang, P. Zhang, J. Qiu, R. Yang, L. Zhou, Development and evaluation of an up-converting phosphor technology-based lateral flow assay for rapid and quantitative detection of aflatoxin B1 in crops, Talanta 161 (2016) 297–303, https://doi.org/10.1016/j.talanta.2016.08.058.